



## Numerical study of corrosion of ferritic/martensitic steels in the flowing PbLi with and without a magnetic field

Sergey Smolentsev<sup>a,\*</sup>, Sheida Saedi<sup>a</sup>, Siegfried Malang<sup>b</sup>, Mohamed Abdou<sup>a</sup>

<sup>a</sup> University of California, LA, United States

<sup>b</sup> Fliederweg 3, D76351 Linckenheim-Hochstetten, Germany

### ARTICLE INFO

#### Article history:

Received 12 April 2012

Accepted 23 August 2012

Available online 7 September 2012

### ABSTRACT

A computational suite called TRANSMAG has been developed to address corrosion of ferritic/martensitic steels and associated transport of corrosion products in the eutectic alloy PbLi as applied to blankets of a fusion power reactor. The computational approach is based on simultaneous solution of flow, energy and mass transfer equations with or without a magnetic field, assuming mass transfer controlled corrosion and uniform dissolution of iron in the flowing PbLi. First, the new tool is applied to solve an inverse mass transfer problem, where the saturation concentration of iron in PbLi at temperatures up to 550 °C is reconstructed from the experimental data on corrosion in turbulent flows without a magnetic field. As a result, a new correlation for the saturation concentration  $C^S$  has been obtained in the form  $C^S = e^{13.604 - 12975/T}$ , where  $T$  is the temperature of PbLi in K and  $C^S$  is in wppm. Second, the new correlation is used in the computations of corrosion in laminar flows in a rectangular duct in the presence of a strong transverse magnetic field. As shown, the mass loss increases with the magnetic field such that the corrosion rate in the presence of a magnetic field can be a few times higher compared to purely hydrodynamic flows. In addition, the corrosion behavior was found to be different between the side wall of the duct (parallel to the magnetic field) and the Hartmann wall (perpendicular to the magnetic field) due to formation of high-velocity jets at the side walls. The side walls experience a stronger corrosion attack demonstrating a mass loss up to 2–3 times higher compared to the Hartmann walls. Also, computations of the mass loss are performed to characterize the effect of the temperature (400–550 °C) and the flow velocity (0.1–1 m/s) on corrosion in the presence of a strong 5 T magnetic field prototypic to the outboard blanket conditions.

© 2012 Elsevier B.V. All rights reserved.

### 1. Introduction

Lead–lithium (PbLi) eutectic alloy and advanced reduced activation ferritic/martensitic (RAFM) steel, such as F82H or EUROFER, are envisaged as practical candidates for using in breeding blankets of a fusion power reactor as a breeder/coolant and a structural material respectively. Implementation of these materials in blanket applications still requires material compatibility studies as many questions related to physical/chemical interactions between PbLi and RAFM steels as well as earlier ferritic/martensitic steels remain to be answered (see, e.g. [1]). First of all, the mass loss caused by the flow-induced corrosion of the steel walls in the flowing PbLi at temperatures in the range 450–550 °C, relevant to blanket operation conditions needs to be characterized. Present PbLi blanket studies limit the maximum wall thinning to 20 μm/yr that corresponds to the maximum wall temperature at the interface with the liquid metal in the hot leg of about 470 °C. These limits were derived in the past in the US in the Blanket Comparison

and Selection Study (BCSS) based on experience with sodium loops, where blocking of the liquid metal circuit by precipitated corrosion products was frequently observed in the cold section of the loop (see, e.g. [2]). The experimental data on the mass loss for ferritic/martensitic steels in the flowing PbLi vary however over a wide range, predicting possible wall thinning at temperatures higher than 450 °C from 20 μm/yr [3] to 900 μm/yr [4] (see also Table 1).

Along with a possible deterioration of the mechanical integrity of the blanket structure due to the wall thinning at the interface with the flowing PbLi, there are other serious concerns associated with the transport of corrosion products throughout the liquid metal loop. When transported with the flowing PbLi in the blanket ducts, the corrosion products can be activated by the intense neutron flux. Their precipitation in the cold part of the PbLi loop, e.g. in a heat exchanger, may lead to considerable safety problems, particularly if deposition of corrosion products results in localized regions of high concentration of activated materials. Plugging the loop by precipitated corrosion products in the cold section is another concern. Such an event has been reported in many experimental studies (see, e.g. [5–7]). At present, it is widely assumed that deposition processes in the cooler parts of a loop are more

\* Corresponding author.

E-mail address: [sergey@fusion.ucla.edu](mailto:sergey@fusion.ucla.edu) (S. Smolentsev).

**Table 1**

Corrosion rate of ferritic/martensitic steels in the flowing PbLi.

Steel	$T_{\max}$ (°C)	Flow regime	Corrosion rate ( $\mu\text{m}/\text{yr}$ )	B field	Reference
Fe-12Cr-1MoVW	500	Laminar	24	–	Tortorelli and De Van [22]
HT-9, Fe-9CR	482	Laminar	20	–	Chopra and Smith [3]
1.4914	550	Turbulent	370	–	Borgstedt and Grundmann [23]
1.4914, HT9, T91	450	Laminar	30	–	Broc et al. [24]
1.4914	475	Turbulent	40	–	Sannier et al. [16]
MANET-1, OPTIFER, F82H	480	Turbulent	100	–	Glasbrenner et al. [25]
EUROFER 97	480	Laminar	40	–	Benamati et al. [26]
EUROFER	550	Laminar	237–530	–	Buceniaks et al. [4]
EUROFER	550	Laminar	550–900	1.7 T	Buceniaks et al. [4]
EUROFER, MANET I, OPTIFER IVa, F82H-mod.	480	Turbulent	90	–	Konys et al. [14]
EUROFER, MANET I, OPTIFER IVa, F82H-mod.	550	Turbulent	400	–	Konys et al. [14]

critical to the safe blanket operation than reduction of strength by wall thinning in the hotter parts. In any case, the corrosion data are required to address transport of corrosion products throughout the liquid metal loop, in particular, to address their deposition in the cold section.

The observed variations in the experimental data on corrosion in the ferritic/martensitic steel–PbLi system point to a strong influence of the interface temperature and, what is also important, of the flow itself, including flow development effects, and especially turbulence and magnetohydrodynamic (MHD) phenomena [4]. Although the influence of the temperature on corrosion processes is known to be described well with a kind of Arrhenius law, the flow effects are poorly understood. The existing experimental data are in fact not sufficient to explain the strong variations in the corrosion rate, first of all due to uncertainties related to different flow conditions in the experiments. Moreover, these experimental data are mostly limited to purely hydrodynamic flows and thus cannot be used to predict corrosion processes and transport of corrosion products in a real blanket system, where the flowing PbLi is severely affected by a strong plasma confining magnetic field. General discussion of possible effects of a magnetic field on corrosion and deposition in PbLi is given in [8]. The main effect of the magnetic field on corrosion processes seems to be due to changes in the velocity profile, mostly due to steeper velocity gradients in the near-wall region and associated changes in the temperature distribution in the flow and at the material interface with the solid metal. Only a few experimental studies [4,9–11] have been performed in the presence of a magnetic field, predicting significant increase in the wall mass loss, up to 2–3 times, if a magnetic field is applied. These results still need to be explained and/or reexamined. This necessitates further experimental and modeling efforts, including development and testing of phenomenological models and boundary conditions followed by new numerical codes and multi-parameter computations.

A few numerical codes, mostly 1D, have been developed in the recent past to simulate transport of corrosion products in big multi-component industrial-type water-cooled and liquid-metal-cooled loops [12,13] for cooling fusion and fission reactor systems. A typical example of the 1D codes is the MATLIM code developed at FZKA [7,14], where the mass transfer equation is reduced to the 1D form by integrating the original 3D equations over the cross-sectional area of the duct. The code had demonstrated a good match with the experimental data for mass loss in hydrodynamic turbulent flows obtained in the past (see, e.g. [15,16] and more recently [7,17,18]). The range of applicability of the code is however limited due to the uncertainties in the input data, such as the diffusion coefficient, solubility of iron in PbLi, and the mass transfer coefficient (private communication with J. Konys, September 2011). Of them, the saturation concentration seems to be the most uncertain parameter, demonstrating scattering up to four orders of magnitude. The code also lacks MHD effects and detailed representation

of the velocity field due to its 1D nature. There are also a few multi-dimensional research codes [19,20] that address special effects associated with the flow geometry, for example, those due to the insulating flow channel insert (FCI) in a dual-coolant DCLL blanket [21], where PbLi is used as a breeder and a coolant, while the helium gas is used for cooling the RAFM steel structure.

In this article we report about our ongoing work on modeling flow-induced corrosion processes in the ferritic/martensitic steel–PbLi system. Two new computer codes have been developed that solve simultaneously the fluid flow, energy and mass transfer equations for either turbulent or laminar flows with or without a magnetic field. The code for turbulent flows is 2D. The simulations we perform using this code are mostly aimed at improving the existing data on the saturation concentration. In order to do this, we solve an inverse problem where the data on saturation concentration of iron in PbLi is reconstructed by comparing calculated results for the mass loss with the available experimental data. The second code covers the case of laminar MHD flows in an electrically conducting rectangular duct. This code utilizes a model of a fully developed 2D MHD flow, while the mass and heat transfer equations are solved in 3D. The obtained data on the saturation concentration are then approximated with a new correlation, which is further used to perform more analysis and comparisons, in particular to address the effects of the magnetic field, temperature and the flow velocity on the mass loss in MHD duct flows.

## 2. Physical model

Various experimental studies in the past [15,16,22–25] as well as more recent experimental data [7,14,17,18,26] have demonstrated two distinct phases in the corrosion process. First, relatively slow dissolution of the passivating oxide layer occurs, and then the corrosion rate is considerably increased due to dissolution of the main steel constituents, iron and chromium. The first phase is also known as the “incubation period”. For blankets operating in a steady-state regime, the second phase is obviously more important than the incubation period. The dissolution process in the second phase is linear in time indicating that the corrosion is uniform and the corrosion rate is constant. For this phase, metallographic examinations of the corroded samples performed in the studies cited above have not revealed any other pronounced corrosion mechanisms, such as formation of intermetallic compounds, penetration of liquid metal along grain boundaries or leaching of any particular steel constituents. This is different from the nickel-rich austenitic steels where leaching of high-solubility nickel results in formation of a porous layer at the interface (see, e.g. [16]). It should be noted that some new experimental data, nevertheless, indicate to some occurrence of other corrosion mechanisms rather than pure dissolution (see, e.g. [27,28]), such as corrosion-erosion and grain/sub-grain boundary penetration. These mechanisms are not considered here. Since iron is the major ferritic/martensitic

**Table 2**  
Chemical composition of some ferritic/martensitic steels [7].

Steel	C	Cr	Ni	Mn	W	V	Ta
EUROFER	0.11	8.82	0.02	0.47	1.09	0.20	0.13
MANET I	0.13	10.6	0.87	0.82	–	0.22	–
Optifer IVa	0.11	8.50	–	0.57	1.16	0.23	0.16
F82H-mod.	0.09	7.70	–	0.16	1.95	0.16	0.02

steel constituent (see Table 2), the considerations of corrosion processes at the interface and further transport of corrosion products with the flowing PbLi are often limited to iron only. In these conditions, the transport model can be reduced from the multi-phase flow to a one-phase flow, using a dilution approximation [29]. This approach is also accepted in the present study.

The flow-induced corrosion processes of ferritic/martensitic steel in the PbLi involve several steps as discussed, for example, in [30]. Each step can be described with a simple mass transfer formula, which relates the mass flux of the dissolved iron with the associated concentration difference or concentration gradient. First, separation of atoms from the solid matrix into the liquid occurs due to the difference between the chemical activity (chemical potential) of a particular steel component in the solid and that in the liquid. An associated mass flux from the wall  $I$  ( $\text{kg}/\text{m}^2 \text{ s}$ ) at the solid/liquid interface can be written (see, e.g. [10,31]) as

$$I = k(C^S - C_W), \quad (1)$$

where  $C^S$  ( $\text{kg}/\text{m}^3$ ) is the saturation concentration of iron in PbLi,  $C_W$  is its concentration in the LM at the interface (wall concentration), and  $k$  ( $\text{m}/\text{s}$ ) is the dissolution rate constant. Second, the solute is transported due to diffusion and convection through the boundary layer in the liquid to the flow bulk, where the major transport mechanism is convection. The contribution of diffusion and convection to the transport of the dissolved material in the boundary layer can vary significantly depending on the flow conditions, such as the flow regime (laminar or turbulent), presence or absence of the magnetic field and the thickness of the concentration boundary layer compared to the thickness of the dynamic boundary layer. The diffusion–convection transport through the boundary layer is usually combined into one mass flux, which can be described with the following mass transfer equation:

$$I = K(C_W - C_b), \quad (2)$$

where  $C_b$  is the concentration of iron in the bulk and  $K$  ( $\text{m}/\text{s}$ ) is the mass transfer coefficient. Due to mass conservation, the two fluxes are equal so that

$$k(C^S - C_W) = K(C_W - C_b). \quad (3)$$

The bulk concentration can be neglected in most cases compared to the wall concentration, thus

$$C_W = C^S(1 + K/k)^{-1}. \quad (4)$$

Eq. (4) shows that the wall concentration is close to the saturation concentration, providing the dissolution rate of iron in PbLi at the interface is much higher than the rate at which the dissolved iron is carried from the solid into the liquid bulk, i.e., when  $K/k \ll 1$ . The last assumption has been confirmed in many experimental studies of the flow-induced corrosion of steels in lead alloys, including PbLi and PbWi (for references see, e.g. [30]). In such a mass transfer controlled regime Eq. (4) can be simplified to

$$C_W = C^S \quad (5)$$

and then used as a boundary condition in the computations of the concentration field. More general third type boundary conditions can also be obtained by equating the mass fluxes:

$$D \frac{\partial C}{\partial n} \Big|_W = k(C^S - C_W), \quad (6a)$$

or

$$D \frac{\partial C}{\partial n} \Big|_W = K(C_W - C_b). \quad (6b)$$

Here,  $D$  ( $\text{m}^2/\text{s}$ ) is the diffusion coefficient of iron in PbLi. Similarly to several other studies (see, e.g. [19,20]), in almost all computations in the present study, we apply a first type boundary condition in the form of Eq. (5).

### 3. Available correlations for saturation concentration of iron in PbLi

As seen from Eqs. (5) and (6) the saturation concentration of iron in PbLi is one of the most important parameters in the corrosion model, which needs to be specified with high enough accuracy. Although several empirical correlations are available, they suggest very different values of  $C^S$ , which vary by several orders of magnitude. All correlations have the same form of Arrhenius-type equation  $C^S = e^{A-B/T}$ , where  $T$  (K) is the absolute temperature, but the parameters  $A$  and  $B$  vary significantly. The data on the solubility of iron in PbLi proposed by Barker et al. [32] were obtained by immersion tests of pure iron in PbLi to determine the concentration of the dissolved metal in a liquid alloy using atomic absorption spectroscopy. These experiments were carried out at different temperatures, such that an expression of variation of the iron solubility with temperature was established as follows:

$$C^S = e^{5.81172 - 1508.35/T}. \quad (7)$$

Borgstedt and Grundmann [23] deduced the iron solubility from dissolution tests in flowing PbLi using a certain correlation for the mass transfer coefficient and certain values for the iron diffusivity based on the Sutherland–Einstein equation. The solubility values by Borgstedt et al. are close to those in pure lead:

$$C^S = e^{24.7136 - 21517.7/T}. \quad (8)$$

The solubility of iron in Pb–17Li was also determined by Feuerstien et al. by dissolution tests in crucibles [33]. For tests done with alpha-iron the following correlation has been obtained:

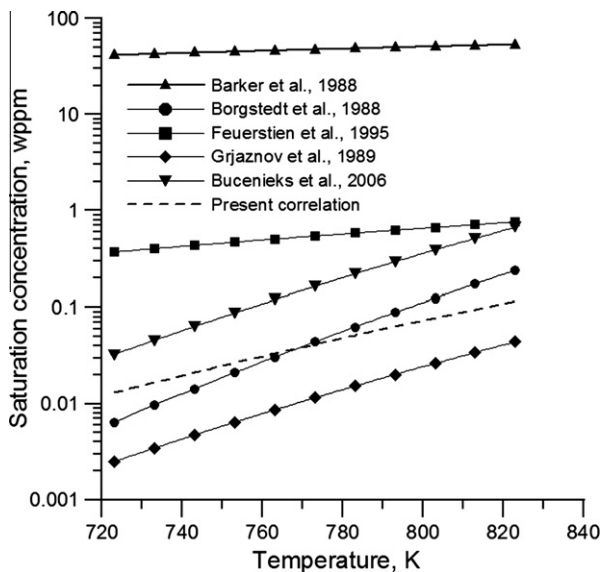


**Fig. 1.** Several correlations for saturation concentration of iron in PbLi as a function of temperature, including a new correlation developed in the present study.

$$C^S = e^{4.94 - 4292/T} \quad (9)$$

Also a correlation for saturation concentration was proposed by Grjaznov et al. [31]:

$$C^S = e^{17.6562 - 17099/T} \quad (10)$$

Recently, Buceniekis et al. have proposed a correlation, using experimental data on the mass loss of EUROFER samples in a laminar flow with and without a magnetic field [4]:

$$C^S = e^{21.47 - 18000/T} \quad (11)$$

In all formulas in this section, the saturation concentration is in wppm. The correlations are illustrated in Fig. 1. Of them, one by Barker et al. [32] gives saturation concentration much higher compared to others, making the difference between the lowest and highest predicted values about four order of magnitude. Other correlations are closer to one another but the uncertainty is still unacceptably high, up to two orders of magnitude. This uncertainty significantly limits the reliability of any theoretical predictions of mass loss where these correlations are used.

#### 4. Mathematical models and numerical codes

Two particular flow scenarios are considered and correspondingly two numerical codes are developed for: (i) turbulent hydrodynamic flow in a pipe or a plane channel and (ii) laminar MHD flow in an electrically conducting rectangular duct. In both cases, the mathematical model includes the fluid flow equations, the energy equation and the mass transfer equation. The mass transfer equation is written in the dilution approximation, assuming all corrosion products are fully dissolved in the liquid metal. In the case of the MHD flow in a rectangular duct, an additional induction equation is used to compute the induced magnetic field  $B_x$  (T), which is further used in computations of the electromagnetic force acting on the liquid.

The main assumptions of the models are discussed in Section 2 and are also summarized here. The models deal with the flow induced corrosion, assuming uniform dissolution of iron in the flowing PbLi. The velocities are relatively low, such that the corrosion rate is mostly controlled by mass transfer processes. At high velocities, higher corrosion rates can be expected due to effect of erosion ([30]). Most of the experimental studies performed in liquid metals (usually for turbulent flows) confirm that the corrosion process is controlled by mass transfer (see, e.g. discussion in [30]). However, the studied velocity range in these experiments is narrow, for instance in the case of PbLi flows, the maximum velocity did not exceed 0.3 m/s. The present model can likely be applied to velocities higher than 0.3 m/s providing that erosion–corrosion does not occur or at least it is insignificant compared to the contribution of the dissolution mechanism. Based on these limitations, all computations for turbulent flows without a magnetic field in this study are limited to the maximum velocity of 0.3 m/s. The other parameters in the computations, the temperature and the channel size, are also comparable with those in experiments to assure model applicability. In the case of MHD flows, flow laminarization typically occurs due to the effect of the applied magnetic field. In such MHD cases, the maximum velocity in the computations was increased to up to 1 m/s (see computations in Section 5.3) as erosion occurrence seems to be unlikely.

The initial iron concentration in all computations in the present study is always assumed to be zero:  $C = 0$  at  $x = 0$ . In computations, the diffusion coefficient of iron in PbLi is calculated using the Sutherland–Einstein equation [7]. For example, using this equation at 550 °C,  $D = 6.4 \times 10^{-9}$  m<sup>2</sup>/s. Other physical properties of PbLi at

this temperature are density 9280 kg/m<sup>3</sup>, kinematic viscosity  $1.1 \times 10^{-7}$  m<sup>2</sup>/s and electrical conductivity  $0.73 \times 10^6$  S/m. The computations are performed in the temperature range from 400 °C to 550 °C taking the temperature variations in the physical properties of PbLi into account based on the PbLi material database in [34]. The two codes have been combined into one computational package called “TRANSMAG” (TRANSport phenomena in MAGneto-hydrodynamic flows). More capabilities, first of all those related to the effect of a magnetic field, will be added to TRANSMAG in the future.

##### 4.1. Turbulent hydrodynamic flows

The transport model is written here in the boundary-layer approximation, which agrees well with the experimental conditions reported in almost all experimental studies, where corrosion specimens were placed inside a long host duct. In such conditions, the diffusion flux in the flow direction can be neglected compared to the convective transport in the same direction. The governing equations that utilize the boundary-layer approximation include the momentum (12), continuity (13), energy (14) and mass transfer (15) equations, which are written in terms of the velocity components  $U$  and  $V$  (m/s), temperature  $T$  (K), pressure  $P$  (Pa) and iron concentration  $C$  (kg/m<sup>3</sup>) in PbLi as follows:

$$\frac{\partial U}{\partial t} + U \frac{\partial U}{\partial x} + V \frac{\partial U}{\partial y} = -\frac{1}{\rho} \frac{\partial P}{\partial x} + \frac{1}{y^m} \frac{\partial}{\partial y} \left[ y^m (v + v_t) \frac{\partial U}{\partial y} \right], \quad (12)$$

$$\frac{\partial U}{\partial x} + \frac{1}{y^m} \frac{\partial}{\partial y} (y^m V) = 0, \quad (13)$$

$$\rho C_p \left( \frac{\partial T}{\partial t} + U \frac{\partial T}{\partial x} + V \frac{\partial T}{\partial y} \right) = \frac{1}{y^m} \frac{\partial}{\partial y} \left[ y^m (\lambda + \lambda_t) \frac{\partial T}{\partial y} \right], \quad (14)$$

$$\frac{\partial C}{\partial t} + U \frac{\partial C}{\partial x} + V \frac{\partial C}{\partial y} = \frac{1}{y^m} \frac{\partial}{\partial y} \left[ y^m (D + D_t) \frac{\partial C}{\partial y} \right]. \quad (15)$$

Here,  $t$  (s) is the time,  $x$  and  $y$  (m) are the coordinates along and across the flow. The integer parameter  $m$  is either 1 (plane channel) or 2 (circular pipe),  $\rho$  (kg/m<sup>3</sup>),  $\nu$  (m<sup>2</sup>/s),  $\lambda$  (W/mK) and  $D$  (m<sup>2</sup>/s) are the fluid density, kinematic viscosity, thermal conductivity and diffusion coefficient of iron in PbLi, while  $v_t$ ,  $\lambda_t$  and  $D_t$  are the turbulent transport properties, which are calculated using a well-known  $k$ – $\varepsilon$  model of turbulence [35]. A numerical code that solves Eqs. (12)–(14) along with the transport equations for the turbulent kinetic energy  $k$  and dissipation rate  $\varepsilon$  (not shown here) was developed in [36]. A new code extends previous code [36] by solving in addition Eq. (15). All equations are approximated with the finite-difference formulas using a stretched grid, which clusters the grid points near the walls. To provide a proper resolution in the wall vicinity, the number of grid points across the flow is 50–200 depending on the Reynolds number, of which at least 10 points are placed within the viscous sublayer. The solution is sought as a steady state of the original time-dependent problem using a Blottner-type finite-difference method [37].

##### 4.2. Laminar flow in a rectangular duct with and without a magnetic field

The mathematical model describes coupled fluid flow, electromagnetic, and heat and mass transfer processes in laminar liquid metal MHD flows in an electrically conducting rectangular duct. Here, we assume fully developed flow conditions, so that 2D MHD equations can be used, while the heat transfer and mass transfer equations are 3D:

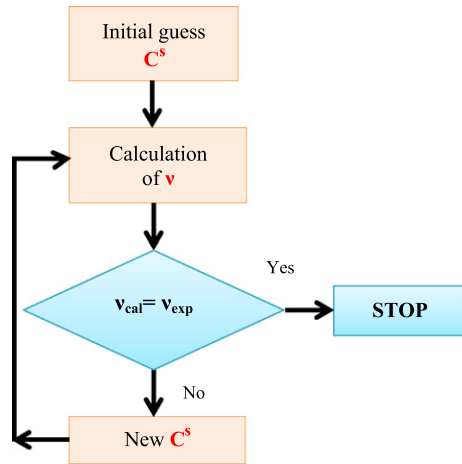


Fig. 2. An algorithm for solving the one-parameter mass transfer problem to reconstruct the saturation concentration data from the experimental data.

$$\frac{\partial^2 U}{\partial z^2} + \frac{\partial^2 U}{\partial y^2} + \frac{B_0}{\nu \rho \mu_0} \frac{\partial B_x}{\partial z} - \frac{1}{\nu \rho} \frac{dP}{dx} = 0, \quad (16)$$

$$U \frac{\partial C}{\partial x} = D \left( \frac{\partial^2 C}{\partial x^2} + \frac{\partial^2 C}{\partial y^2} + \frac{\partial^2 C}{\partial z^2} \right), \quad (17)$$

$$\frac{1}{\mu_0} \frac{\partial}{\partial z} \left( \frac{1}{\sigma} \frac{\partial B_x}{\partial z} \right) + \frac{1}{\mu_0} \frac{\partial}{\partial y} \left( \frac{1}{\sigma} \frac{\partial B_x}{\partial y} \right) + B_z^0 \frac{\partial U}{\partial z} = 0, \quad (18)$$

$$\rho C_p U \frac{\partial T}{\partial x} = \frac{\partial}{\partial x} \left( k \frac{\partial T}{\partial x} \right) + \frac{\partial}{\partial y} \left( k \frac{\partial T}{\partial y} \right) + \frac{\partial}{\partial z} \left( k \frac{\partial T}{\partial z} \right). \quad (19)$$

Here,  $B_0$  is the applied constant (transverse) magnetic field,  $\sigma$  (S/m) is the electrical conductivity, and  $\mu_0$  (H/m) is the magnetic permeability of vacuum. When solving the whole problem, the momentum Eq. (16) and the mass transfer Eq. (17) are solved in the liquid only, while the induction Eq. (18) and heat transfer Eq. (19) are integrated over the whole domain, including the conducting walls. The induced magnetic field enters the momentum equation through the flow-opposing Lorentz force term. The boundary condition on the velocity is a no-slip condition at the interface between the liquid and solid. The external boundary condition on the induced magnetic field at the interface between the duct wall and the surrounding non-conducting medium is  $B_x = 0$  to assure that the magnetic field does not diffuse into the outer region. This mathematical model was previously used in computations of MHD flows, heat transfer and tritium transport in poloidal ducts of the DCLL blanket in [38,39].

The numerical code uses a control-volume technique based on non-uniform collocated Cartesian meshes. Both the velocity and magnetic field are defined at the center of the control-volume cell, while the fluxes are defined at the center of the cell side. The mesh is non-uniform, clustering points in the Hartmann layers at the walls perpendicular to the applied magnetic field and in the side layers at the walls parallel to the field. Typically, the total number of the mesh points in the cross-sectional area is 151 by 151, which includes about 25 points in the wall and at least 10 points within the Hartmann and side layers. The code solves finite-difference equations obtained from Eqs. (16)–(19) using the ADI (Alternative Direction Implicit) method [40] until a steady-state solution is reached. Then, the velocity distribution is used as an input data to solve the 3D mass and heat transfer equations using an explicit method.

## 5. Results and discussion

### 5.1. Turbulent flows

First, the code for turbulent flows described in Section 4.1 is applied to solve a one-parameter inverse problem to obtain a new correlation for the saturation concentration  $C^s$  of iron in PbLi by matching calculated and experimental data on corrosion of martensitic steels in the flowing PbLi. The experimental data used in this matching procedure are the corrosion rates  $v$  ( $\mu\text{m}/\text{yr}$ ), which are summarized in [15] in the form of a semi-empirical correlation known as Sannier's equation:

$$v = 8 \times 10^9 \times \text{Exp} \left[ -\frac{25690}{1.98T} \right] \times U_m^{0.875} \times D_h^{-0.125}, \quad \mu\text{m}/\text{yr}. \quad (20)$$

Here,  $T$  is the absolute temperature of the flowing PbLi in K,  $U_m$  is the flow velocity in m/s and  $D_h$  is the hydraulic diameter in m. This formula is based on the approximation of the experimental data obtained in [15] and also uses earlier experimental data cited in [15]. The equation is applicable to fully developed turbulent flows of PbLi. The effect of the position on the corrosion rate has also been addressed in [15]. It appears that over the major length of the hot zone where the temperature is uniform (1 m in [15]), the corrosion rate is uniform, except for a short 10-cm region at the channel inlet, where it is higher compared to the rest of the hot zone. Therefore, the formula is not applicable to the short inlet section. Some recent studies [14] have also confirmed the applicability of Sannier's equation to the temperatures as high as 550 °C.

The major steps in the solution of the suggested inverse problem are illustrated in Fig. 2. As a first step, the Borgstedt's correlation (8) is used as an initial guess for the saturation concentration. After solving the transport problem, the calculated concentration field is used to calculate corrosion rate  $v_{cal}$ , which is then compared with  $v_{exp}$  calculated with Eq. (20), and then  $C^s$  is adjusted to minimize the difference between  $v_{cal}$  and  $v_{exp}$ . This procedure is repeated several times until condition  $v_{cal} = v_{exp}$  is matched. In agreement with the experimental observations, the corrosion rate computed numerically is higher over a short inlet section and then drops downstream to some value, which does not experience further changes with the distance. Some examples of such behavior typical to heat and mass transfer in long ducts can be seen in Fig. 7. This asymptotic value of the corrosion rate is used as  $v_{cal}$ . Finally, the values of the saturation concentration that resulted in a good match between the experimental and numerical data in the reference temperature range are used to construct a new correlation for  $C^s$  versus the temperature in the form  $C^s = e^{A-B/T}$ .

In the present computations, when solving the inverse problem, the hydraulic diameter and the flow velocity are fixed to some values from the middle of the parameter range reported in the experimental studies. Namely,  $D_h = 0.02$  m and  $U_m = 0.11$  m/s, while the temperature is varied from 450 °C to 550 °C. The effect of  $D_h$  and  $U_m$  on corrosion is also addressed in further computations. Tuning  $C^s$  via comparisons between the computed mass losses and those from Sannier's equation as suggested in Fig. 2 has resulted in the following correlation:

$$C^s = e^{13.604 - 12975/T}, \quad (21)$$

which is also plotted in Fig. 1. Among all correlations plotted in this figure, the one from Borgstedt is the nearest to the new correlation. For temperatures below 500 °C the new correlation gives higher values of  $C^s$  compared to Borgstedt's correlation while for higher temperatures the new data are smaller. The correlation by Grjaznov et al. is the second nearest to the new one but it predicts smaller values in the whole temperature range compared to Eq. (21).

Fig. 3 shows the computed wall thinning ( $\mu\text{m}/\text{yr}$ ) as a function of the PbLi temperature using three correlations, including the new

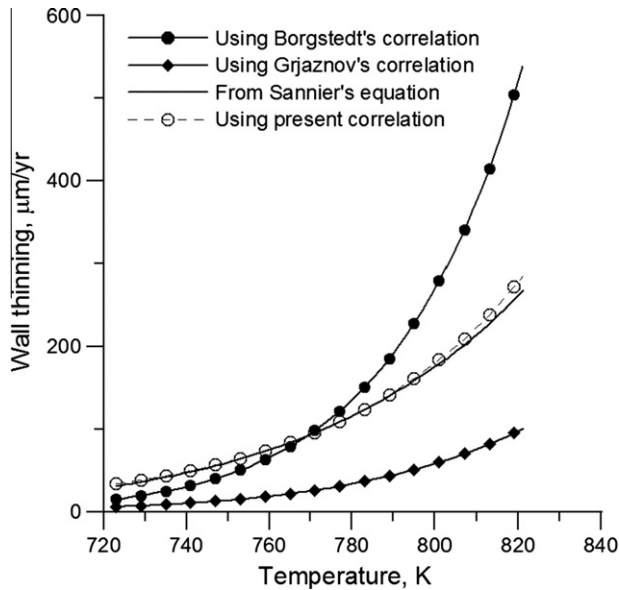


Fig. 3. The wall thinning versus temperature with 3 correlations for the saturation concentration, including the present one, Eq. (21), at  $U_m = 0.11$  m/s,  $D_h = 0.02$  m.

one. The wall thinning is shown at some distance from the flow inlet where the corrosion rate is uniform to match the experimental conditions. Using either the empirical correlation for saturation concentration by Borgstedt or that by Grjaznov along with the first type boundary condition does not lead to a good fit with Sannier's equation. Some computations were also performed using a more general boundary condition of the third type, Eq. (6). In these computations the optimal values of two parameters  $k$  and  $C^S$  were sought to minimize the difference between the computed mass loss and that from Sannier's equation. In most of the cases, applying correlations (8) and (10) does not result in any reasonable match. In fact, using Borgstedt's correlation allows for the optimal values of  $k$  and  $C^S$  only for temperatures above 500 °C. Using both Borgstedt's correlation below 500 °C and Grijaznov's correlation in

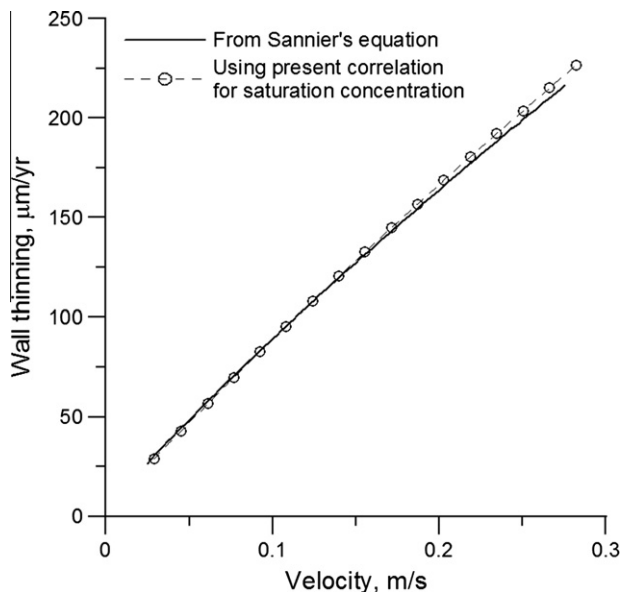


Fig. 4. Wall thinning as a function of velocity at  $T = 500$  °C,  $D_h = 0.02$  m compared to Sannier's equation. The present correlation for saturation concentration, Eq. (21), is used.

the temperature range from 450 °C to 550 °C underpredicts the corrosion rate regardless of  $k$  and  $C^S$ . In those cases where a good match was found using Borgstedt's correlation, the wall concentration was observed to be close to the saturation concentration with a maximum difference of about 20%. These observations are in fact indirect evidences in favor of the first type boundary condition.

The new correlation is then used in the computations of the mass transfer problem to calculate the wall thinning as a function of the velocity (Fig. 4), which is the second most important parameter in corrosion processes. Similar to Fig. 3 the data in Fig. 4 are shown for the flow section far from the inlet where the corrosion rate is uniform. As seen from this figure, there is a good match between the computed values and those from Sannier's equation. A good match with Sannier's equation has also been confirmed in the whole range of the parameters (velocity and channel dimension) where this equation is valid, demonstrating a maximum difference of only a few percents.

## 5.2. Laminar flows in a rectangular duct: effect of a magnetic field

The velocity profile is computed first as described in Section 4.2 and then the velocity data are used as input data for the mass transfer code to solve the mass transfer problem applying the new correlation for the saturation concentration (21) as a boundary condition. The main goal of these computations is to address the effect of the magnetic field on the wall thinning. To do this, we consider a fully developed flow of PbLi at 500 °C in a conducting rectangular duct made of RAFM steel with the cross-sectional dimensions  $2b = 2a = 2$  cm, length  $L = 1$  m and the wall thickness  $t_w = 1$  mm. The applied transverse magnetic field  $B_0$  is varied from 0 to 6 T. This corresponds to Hartmann numbers ( $Ha = B_0 b \sqrt{\sigma / (\nu \rho)}$ ) up to 1325. Notice that the Hartmann number is the dimensionless strength of the magnetic field. On the other hand, in magnetohydrodynamics,  $Ha$  is considered as a similarity number such that the Hartmann number squared is the ratio between the electromagnetic (Lorentz) force and the viscous force [41]. In MHD duct flows, the Hartmann number can also be used to characterize the thickness of the MHD boundary layers. The MHD boundary layer at the duct walls perpendicular to the magnetic field, known as the Hartmann layer, has a thickness scaling as  $1/Ha$ , while the boundary layer at the walls parallel to the magnetic field (side or Shercliff layer) scales in thickness as  $1/\sqrt{Ha}$ . Within the MHD boundary layers, the velocity varies exponentially with the distance. The sharp velocity gradients in the MHD boundary layers can be responsible for intensification of transport processes in the liquid compared to purely hydrodynamic flows, where boundary layers are much thicker and the velocity gradients are correspondingly smaller.

Three velocities are considered here:  $U_m = 1, 2$  and 3 cm/s, such that the maximum hydrodynamic Reynolds number ( $Re = U_m 2a / \nu$ ) is 5580. This choice of parameters is typical for the conditions in corrosion experiments and also assures that the flow is laminar as it typically is under blanket conditions (not counting for possible quasi-2D turbulence). In addition to  $Ha$  and  $Re$ , the third dimensionless parameter in this problem is the wall conductance ratio  $c_w = t_w \sigma_w / (b \sigma) = 0.2$ .

The computed velocity profiles (Fig. 5) demonstrate Hartmann layers and formation of high-velocity jets at the side walls, where the flow-opposing Lorentz force is smaller compared to that in the core flow. In this core bounded by the Hartmann layers and the jets, the flow is almost uniform. The peak velocity in the jets is known to scale with the Hartmann number as  $\sqrt{Ha}$ , while the core velocity, as seen in the figure, is close to the mean bulk velocity. In the figure, the velocity is scaled by the bulk velocity  $U_m$ . Such a velocity structure has strong impact on the corrosion processes. One can see a strong effect of the magnetic field on the mean bulk

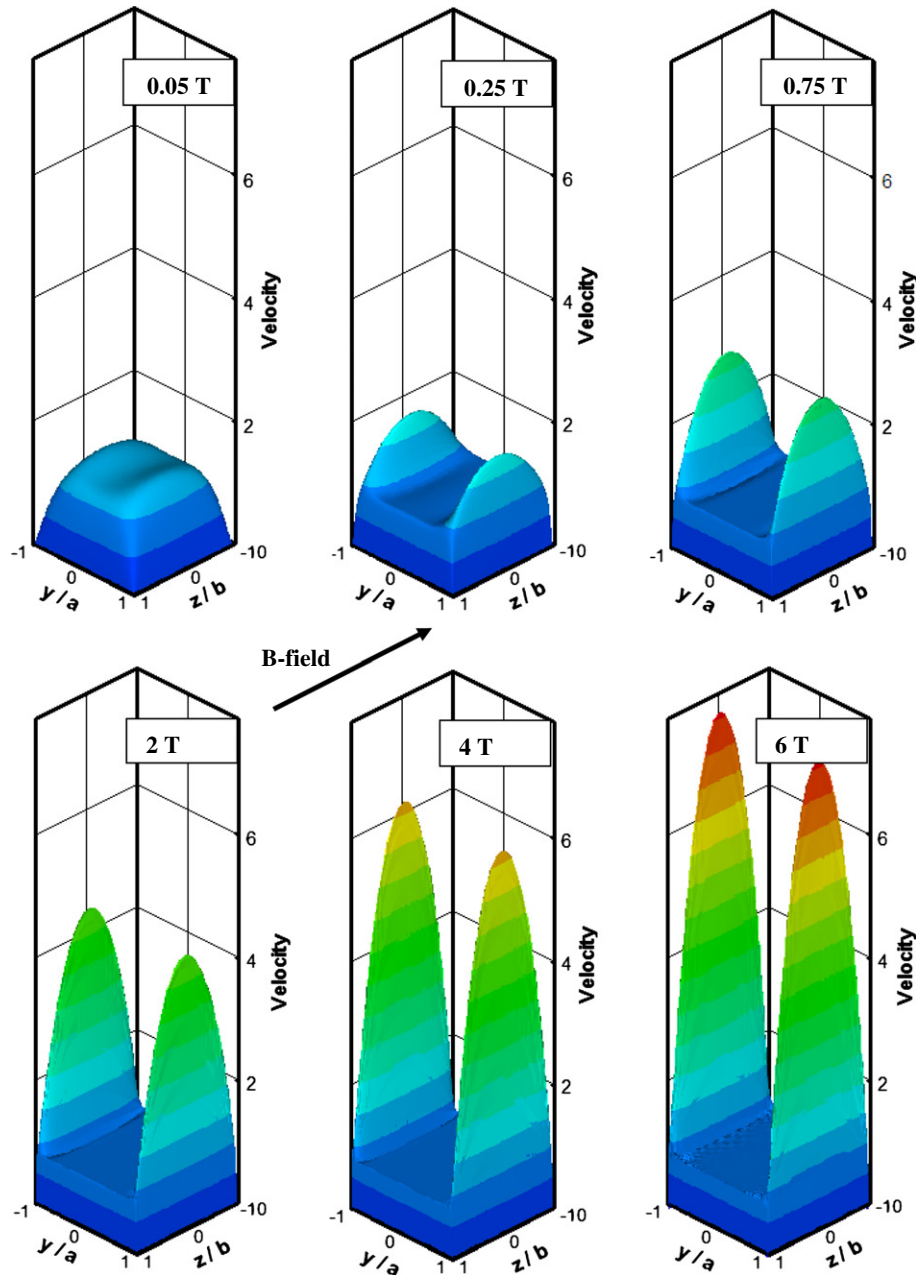


Fig. 5. Effect of the magnetic field on the velocity profile in the reference fully developed MHD flow of PbLi in a square duct at  $c_w = 0.2$ .  $Ha$  changes from 13 to 1325.

concentration (Fig. 6). The higher the magnetic field, the more wall material is dissolved in the flowing liquid. It is obvious that the observed increase in the mass loss with the magnetic field is related to the sharp velocity gradients and high-velocity jets. More detailed analysis of the corrosion mass loss (Fig. 7) shows that the side walls are more affected by corrosion than the Hartmann walls. This difference can be explained by significant differences in the velocity distribution in the near-wall region between the two walls as seen in Fig. 5.

Although the Hartmann layer exhibits higher velocity gradients, the side layer has a higher velocity associated with the near-wall jet. For both walls, large changes in the wall thinning occur within the inlet section of the duct, which varies in length from several centimeters to about half a meter as the magnetic field is increased. Further downstream, variations in the wall thinning are insignificant. The difference in the mass loss between the Hartmann and the side wall is also illustrated in Fig. 8, where the

wall thinning at the end of the 1 m duct section is shown as a function of the magnetic field. The mass loss from the Hartmann wall first increases with the field and then saturates at relatively small  $B_0$  of about 0.2–0.3 T, while the mass loss from the side wall continues to increase with the magnetic field. As a result, the difference in the wall thinning between the two walls increases continuously with the magnetic field up to 3 times at 6 T.

To better understand the observed differences in the wall thinning between the Hartmann and the side walls, more computations are plotted in Figs. 9 and 10. Fig. 9 shows the development of the concentration field along with the thickness of the concentration boundary layer at the Hartmann wall as the liquid proceeds downstream. This thickness is defined using a criterion based on a 1% difference between the local concentration in the liquid and that at the interface. Fig. 10 shows the development of the concentration boundary layer at both the Hartmann and side walls for several values of the applied magnetic field. The thicknesses of

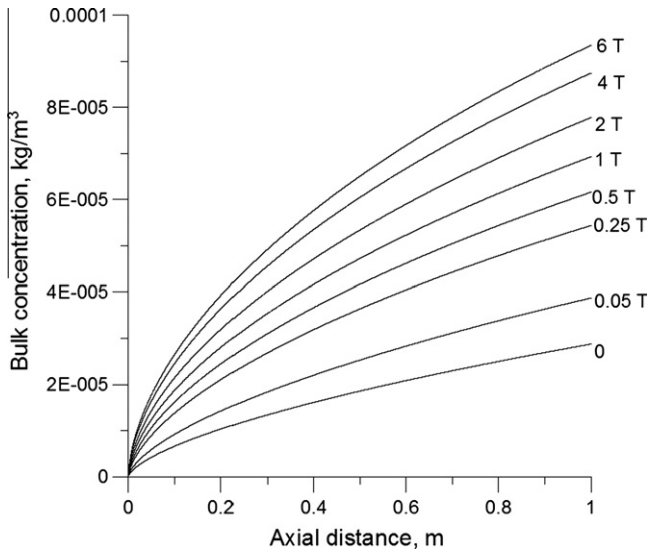


Fig. 6. Increase in the bulk concentration with the axial distance for magnetic fields from 0 to 6 T in the reference MHD flow in a square duct at  $U_m = 1$  cm/s.

the MHD boundary layers are also shown in this figure for  $B_0 = 0.1$  T. One can see that the increase in the magnetic field results in thinning the concentration boundary layer at the side wall. As for the Hartmann wall, the effect of the magnetic field on the thickness of the concentration boundary layer is opposite. However, the magnetic field has a very weak effect on the thickness of the concentration boundary layer at the Hartmann wall except for small values of  $B_0$  around 0.1–0.2 T.

It is noticeable that the concentration boundary layer at the Hartmann wall is much thicker (except for the short inlet section of the duct) than the Hartmann layer. The last observation explains why the mass loss at the Hartmann wall saturates with the magnetic field as demonstrated in Fig. 8. The concentration boundary layer at the side wall is thinner than that at the Hartmann wall but it is comparable in thickness with its counterpart MHD boundary layer. That is why unlike the Hartmann wall no mass loss saturation at the side wall occurs as the magnetic field is increased. One more difference from the Hartmann wall is that the thickness of the concentration boundary layer at the side wall decreases as the magnetic field is increased.

It should be noticed that the present model does not capture some minor effects, such as formation of grooves at the Hartmann

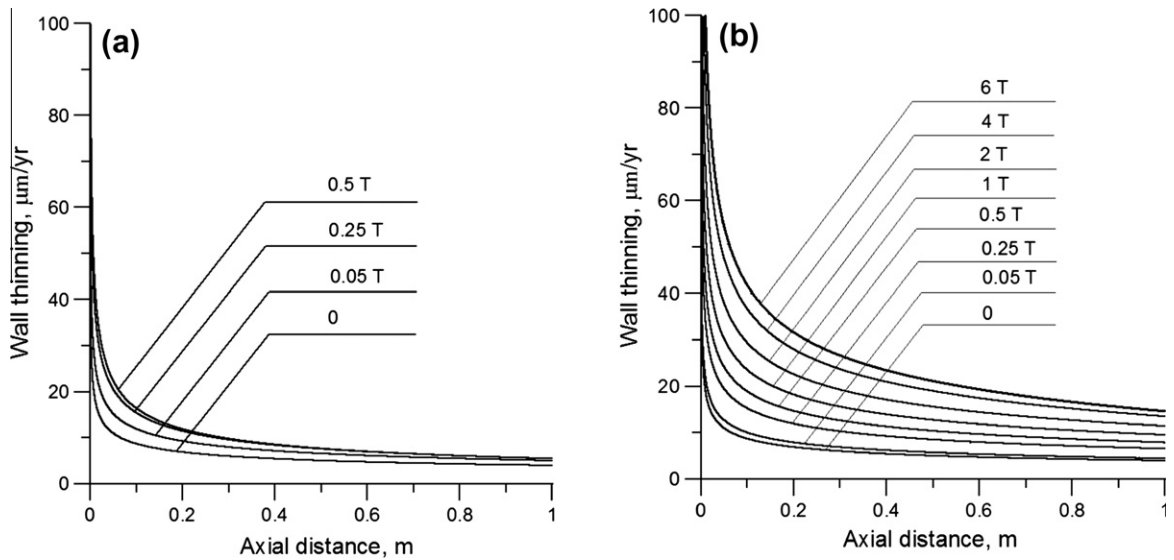


Fig. 7. Wall thinning with the axial distance in the reference MHD flow in a square duct for: (a) Hartmann wall and (b) side wall at  $U_m = 1$  cm/s.

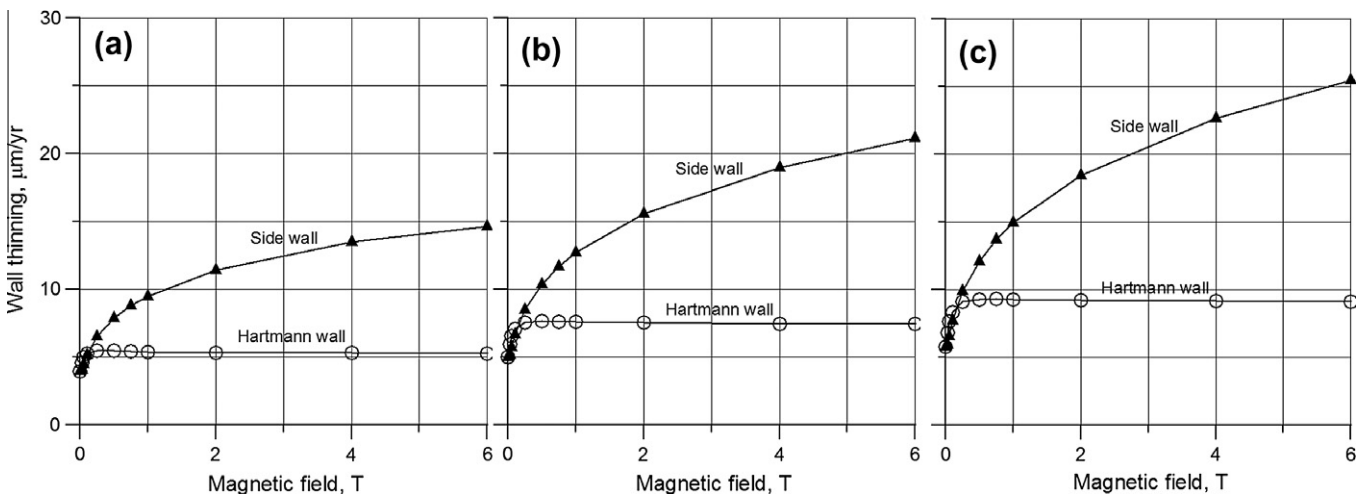
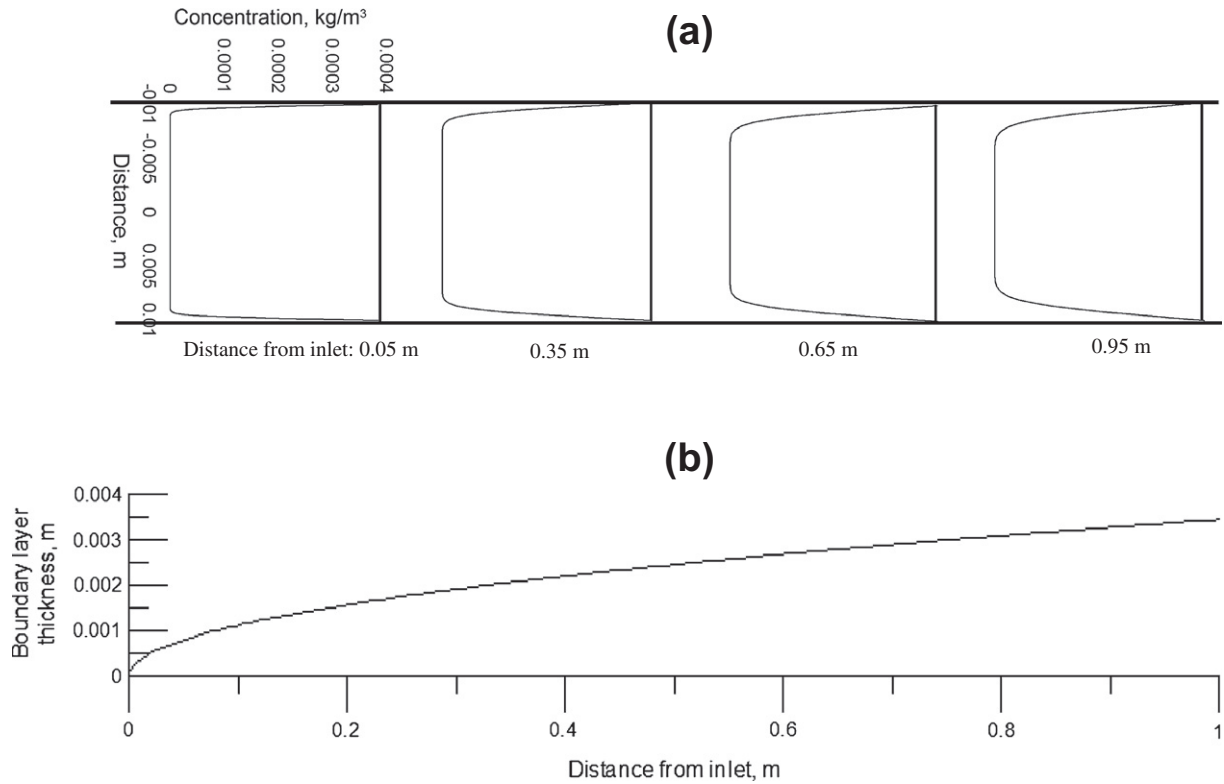


Fig. 8. Difference in the wall thinning at the end of the 1-m section between the Hartmann and the side wall in the reference MHD square duct flow at: (a) 1 cm/s, (b) 2 cm/s and (c) 3 cm/s.



**Fig. 9.** Concentration field in the reference MHD flow in a square duct at  $U_m = 1$  cm/s and  $B_0 = 1$  T: (a) concentration profiles in the duct mid-plane  $y = 0$  parallel to the magnetic field and (b) thickness of the concentration boundary layer at the Hartmann wall.

walls as reported in [4], which seem to be related to unsteady three-dimensional phenomena in the MHD flows as analyzed in [42].

**5.3. Laminar flows in a rectangular duct in a strong magnetic field: effects of temperature and velocity**

In addition to the effect of the magnetic field on the mass loss, here we look at the effect of the temperature and the flow velocity in a rectangular duct, providing a strong magnetic field is applied.

To our best knowledge this is the first time such an analysis was done. In all previous studies the magnetic field was not considered and/or the temperature and the flow velocity were not varied. The reference duct has dimensions  $2b = 2a = 20$  cm,  $L = 2$  m and  $t_w = 5$  mm. The applied transverse magnetic field is 5 T, which matches the toroidal magnetic field in the outboard region of a fusion reactor. The associated Hartmann number is 13230 and the wall conductance ratio is 0.1. These parameters are relevant to self-cooled blanket conditions. It should be noted that a self-cooled PbLi blanket concept was considered in the past and found

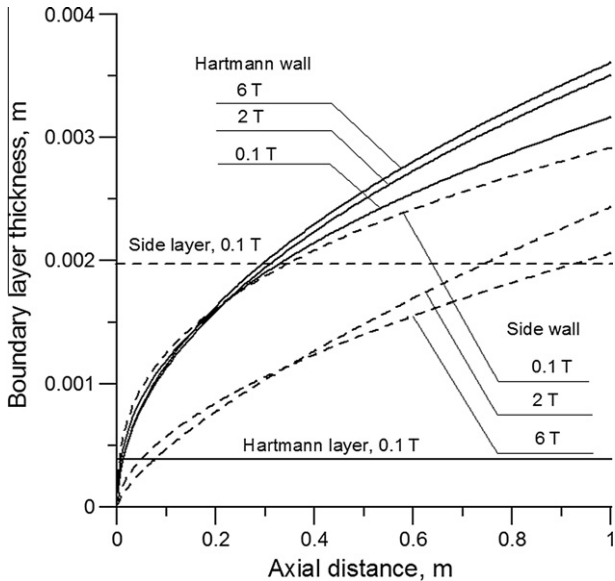


**Fig. 10.** Thickness of the concentration boundary layer as a function of the axial distance in the reference MHD flow in a square duct at the Hartmann and the side wall at  $U_m = 1$  cm/s.

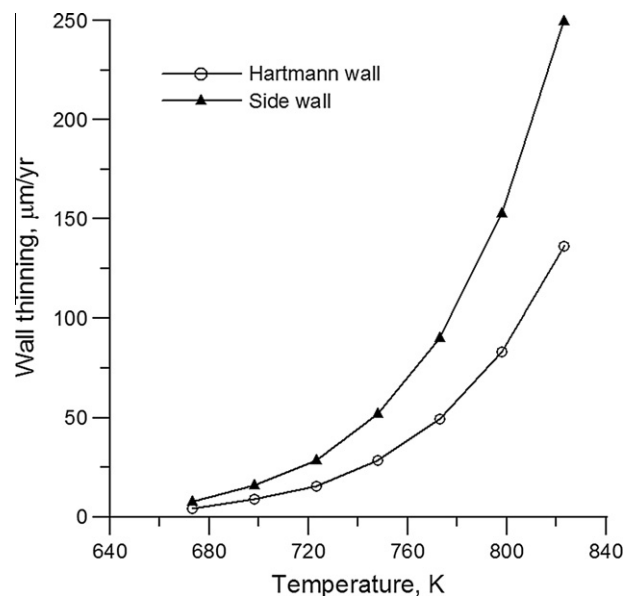


**Fig. 11.** Effect of the temperature on wall thinning averaged over the duct length  $L$  at  $U_m = 0.5$  m/s. Other parameters are given in the text.

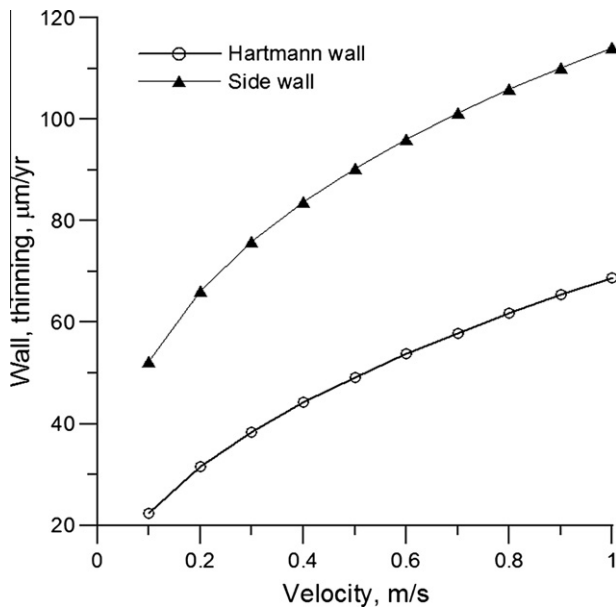


Fig. 12. Effect of the velocity on the wall thinning averaged over the duct length  $L$  at  $T = 500$  °C. Other parameters are given in the text.

promising (see, e.g. [43]), however, currently DCLL and HCLL (Helium-Cooled Lead-Lithium [44]) blanket concepts receive more attention. The flow conditions in these two blankets are different from the self-cooled blanket such that special analysis of the corrosion processes may be needed for them. In particular, in the DCLL blanket, most of the corrosion processes occurs in poloidal flows in a thin gap between the SiC FCI and the host steel duct.

In the present analysis, the velocity and the temperature are used as parameters and varied from 0.1 m/s to 1 m/s and from 400 °C to 550 °C, correspondingly. The computational procedure is similar to that in the previous section. The computed velocity profile has distinguished high-velocity jets at the side walls similar to Fig. 5. All conclusions on the effect of a magnetic field made in the previous section also apply to the reference flow. The results for the wall thinning averaged over the duct length as  $L^{-1} \int_0^L v(x) dx$  are plotted in Figs. 11 and 12 separately for the Hartmann wall and for the side wall. The side wall thinning is always higher compared to the Hartmann wall. As seen from the figures the difference is typically about 2 times. Fig. 11 illustrates the effect of the temperature. As expected, the wall thinning varies exponentially as the temperature is increased. At a velocity of 0.5 m/s the value of 20 µm/yr is exceeded if the temperature is higher than 430 °C. The effect of the velocity at 500 °C is illustrated in Fig. 12. As seen from this figure, the wall thinning increases with the velocity as a power function, i.e., the velocity has a weaker effect on corrosion of both the Hartmann wall and the side wall compared to the temperature. However the velocity effect is still significant. The increase in the velocity from 0.2 m/s to 1 m/s results in doubling the mass loss. These observations suggest scaling laws for the mass loss:  $ML \sim e^{pT} U_m^q B_0^s$  for the side wall, and  $ML \sim e^{pT} U_m^q$  for the Hartmann wall, where  $q, s \sim 0.5$ .

## 6. Concluding remarks

A computational suite called TRANSMAG (TRANSport phenomena in MAGnetohydrodynamic flows) has been developed to address mass transfer processes associated with corrosion of ferritic/martensitic, in particular RAFM, steels in the flowing eutectic alloy PbLi with and without a magnetic field. The new tool

combines two numerical codes: (i) turbulent hydrodynamic flows in a pipe or a plane channel and (ii) laminar MHD flows in an electrically conducting rectangular duct. First, computations were performed to solve a one-parameter inverse mass transfer problem to reconstruct saturation concentration data from the experimental results on corrosion rates in turbulent flows without a magnetic field. These data are then approximated with a new correlation, Eq. (21), which gives the saturation concentration of iron in PbLi as a function of the temperature of the liquid in the form of the Arrhenius-like equation. Using this correlation in computations of corrosion processes has resulted in fair prediction of the wall mass loss for a wide range of flow parameters. The applicability of this correlation has been demonstrated in the temperature range from 450 °C to 550 °C. A good match with the experimental data also suggests the adequacy of the proposed model assumptions, including: mass transfer controlled regime, dilution approximation, one-phase flow and eventually the first type boundary condition in the form of Eq. (5).

Second, the new correlation was used to analyze mass losses in laminar fully developed rectangular duct flows in the presence of a transverse magnetic field. It was found that the corrosion rate under the effect of a strong magnetic field can be a few times higher compared to pure hydrodynamic flows. However, the computations have revealed significant differences in the corrosion behavior between the Hartmann and the side walls. Namely, the side walls are more affected by the corrosion attack due to formation of high-velocity jets in the flow. The observed differences in the mass loss between these two walls are up to 2–3 times. In both cases, the mass loss increases with the magnetic field. However, the mass loss from the Hartmann wall first increases and then saturates, while the mass loss from the side wall is always increasing. This behavior has been explained by the difference in the thickness of the concentration boundary layer at the Hartmann and side walls. In the case of the Hartmann walls, the thickness of the Hartmann boundary layer is smaller than that of the concentration boundary layer, while in the case of the side walls both boundary layers are comparable in thickness. The observed differences in the corrosion behavior between the Hartmann and side walls suggest that in MHD rectangular duct flows, most of the mass loss occurs from the side walls, whereas all experimental studies [4,10,11] have focused on the Hartmann walls.

In another set of computations for laminar flows in a rectangular duct, the effects of the flow velocity and the temperature were analyzed under conditions of a strong, 5 T, transverse magnetic field. For a 0.5-m/s flow in a 2-m long, 20-cm by 20-cm square duct, the wall thinning increases exponentially from 5 to 140 µm/yr for the Hartmann wall and from 8 to 250 µm/yr for the side wall as the temperature is increased from 400 to 550 °C. This analysis suggests scaling laws for the mass loss in rectangular ducts in the form:  $ML \sim e^{pT} U_m^q B_0^s$  for the side wall, and  $ML \sim e^{pT} U_m^q$  for the Hartmann wall, where  $q, s \sim 0.5$ .

The observations made on the effect of a magnetic field on corrosion rate in laminar MHD flows in a rectangular duct are in good qualitative agreement with the experimental data obtained at the Institute of Physics, Latvia (Riga experiment) [4,10,11]. Namely, the increase of the corrosion rate by factor of 2–3 when the magnetic field is applied and much higher corrosion rates at the inlet section can be seen in both experimental and present numerical data. Quantitative comparisons with the experimental data demonstrate, however, significant differences (up to 50%) even for hydrodynamic flows, always showing smaller corrosion rates in computations. These differences may indicate some mismatch between the modeling assumptions and experimental conditions. Taking into account that the available experimental data on corrosion in MHD flows are very limited, and the flow measurements and detailed comparison between the PbLi composition before

and after the experiment in these studies were not done, it is difficult to explain these differences. Therefore, more experimental studies of MHD flow induced corrosion and comparisons with modeling predictions seem to be necessary in the future.

## References

- [1] S. Malang, M. Tillack, C.P.C. Wong, N. Morley, S. Smolentsev, *Fusion of Science and Technology* 60 (2011) 249–256.
- [2] D.L. Smith, C.C. Baker, D.K. Sze, G.D. Morgan, M.A. Abdou, S.J. Piet, S.R. Schultz, R.W. Moir, J.D. Gordon, *Fusion Technology* 8 (1985) 10–113.
- [3] O.K. Chopra, D.L. Smith, *Journal of Nuclear Materials* 141–143 (1986) 566–570.
- [4] I. Bucenies, R. Krishbergs, E. Platacis, G. Lipsbergs, A. Shishko, A. Zik, F. Muktepavela, *Magneto hydrodynamics* 42 (2006) 237–251.
- [5] H.U. Borgstedt, H.D. Röhrig, *Journal of Nuclear Materials* 179–181 (1991) 596–598.
- [6] S. Malang, I.N. Sviatoslavsky, Corrosion product cleanup system for a liquid metal cooled fusion power reactor blanket, in: *Annual Meeting of the American Nuclear Society*, vol. 46, New Orleans, LA, USA, 1984, pp. 289–290.
- [7] W. Krauss, J. Konys, H. Steiner, J. Novotny, Z. Voss, O. Wedemeyer, Development of Modeling Tools to Describe the Corrosion Behavior of Uncoated EUROFER in Flowing Pb–17Li and their Validation by Performing of Corrosion Tests at T up to 550 °C, FZKA 7295, Forschungszentrum Karlsruhe, 2007.
- [8] F. Barbier, A. Alemany, S. Martemianov, *Fusion Engineering and Design* 43 (1988) 199–208.
- [9] A. Terlain, T. Dufrenoy, *Journal of Nuclear Materials* 212–215 (1994) 1504–1508.
- [10] R. Krishbergs, E. Ligere, F. Muktepavela, E. Platacis, A. Shishko, A. Zik, *Magneto hydrodynamics* 45 (2009) 289–296.
- [11] E. Platacis, A. Ziks, A. Poznjak, F. Muktepavela, A. Shishko, S. Sarada, P. Chakraborty, K. Sanjay, M. Vrushank, R. Fotedar, E.K. Rajendra, A.K. Suri, Corrosion phenomena of FMS (P-91) steel in Pb–Li in magnetic field, in: *8th International Pamir Conference on Fundamental and Applied MHD*, Borgo, Corsica, France, vol. 2, September 5–9, 2011, pp. 587–592.
- [12] P.J. Karditsas, C.B.A. Forty, Activation product transport in the helium cooling circuit of the SEAFP plant model 1, in: *16th IEEE/NPSS Symposium on Fusion Engineering*, vol. 2, October 1–5, 1995, Urbana, IL, USA, pp. 1002–1005.
- [13] L. Di Pace, F. Dacquait, P. Schindler, V. Blet, F. Nguyen, Y. Philibert, B. Larat, *Fusion Engineering and Design* 82 (2007) 237–247.
- [14] J. Konys, W. Krauss, H. Steiner, *Fusion of Science and Technology* 56 (2009) 281–288.
- [15] R. Sannier, T. Flament, A. Terlain, Corrosion of martensitic steels in flowing Pb17Li, in: *Proc. 16th Symp. Fusion Tech.*, September 3–7, 1990, London, UK, pp. 901–905.
- [16] J. Sannier, M. Broc, T. Flament, A. Terlain, *Fusion Engineering and Design* 14 (1991) 299–307.
- [17] J. Konys, W. Krauss, Z. Voss, O. Wedemeyer, *Journal of Nuclear Materials* 329–333 (2004) 1379–1383.
- [18] J. Konys, W. Krauss, Z. Voss, O. Wedemeyer, *Journal of Nuclear Materials* 367–370 (2007) 1144–1149.
- [19] S. Malang, D.L. Smith, Modeling of Liquid–Metal Corrosion/Deposition in a Fusion Reactor Blanket, ANL/FPP/TM-192, 1984.
- [20] C. Mistrangelo, MHD and Corrosion Analysis of Dual Coolant PbLi Blanket Modules for ARIES-CS, FZKA 7311, Forschungszentrum Karlsruhe, 2007.
- [21] C.P.C. Wong, S. Malang, M. Sawan, M. Dagher, S. Smolentsev, B. Merrill, M. Youssef, S. Reyes, D.K. Sze, N.B. Morley, S. Sharafat, P. Calderoni, G. Sviatoslavsky, R. Kurtz, P. Fogarty, S. Zinkle, M. Abdou, *Fusion Engineering and Design* 81 (2006) 461–467.
- [22] P.F. Tortorelli, J.H. De Van, *Journal of Nuclear Materials* 141–143 (1986) 592–598.
- [23] H.U. Borgstedt, M. Grundmann, *Fusion Engineering and Design* 6 (1988) 155–158.
- [24] M. Broc, T. Flament, P. Fauvet, J. Sannier, *Journal of Nuclear Materials* 155–157 (1988) 710–714.
- [25] H. Glasbrenner, J. Konys, H.D. Röhrig, *Journal of Nuclear Materials* 283–287 (2000) 1332–1335.
- [26] G. Benamati, C. Fazio, I. Ricapito, *Journal of Nuclear Materials* 307–311 (2011) 1391–1395.
- [27] M. Kondo, T. Nagasaka, T. Muroga, A. Sagara, V. Tsisar, A. Suzuki, T. Terai, M. Takahashi, N. Fujii, T. Yokoyama, H. Miyamoto, E. Nakamura, *Fusion Engineering and Design* 86 (2011) 2500–2503.
- [28] Y.F. Li, M. Kondo, T. Nagasaka, T. Muroga, V. Tsisar, *Fusion of Science and Technology* 60 (2011) 359–363.
- [29] F.P. Incropera, D.P. Dewitt, T.L. Bergman, A.S. Lavine, *Fundamentals of Heat and Mass Transfer*, John Wiley & Sons, 2007.
- [30] F. Balbaud-Céléfier, F. Barbier, *Journal of Nuclear Materials* 289 (2001) 227–242.
- [31] G.M. Grjaznov, V.A. Evtikhin, I. Lyublinski, *Material Science for Liquid Metal Systems of Fusion Reactors*, Energoatomizdat, Moscow, 1989. (in Russian).
- [32] M.G. Barker, V. Coen, H. Kolbe, J.A. Lees, L. Orecchia, T. Sample, *Journal of Nuclear Materials* 155–157 (1988) 732–735.
- [33] H. Feuerstein, H. Gräbner, J. Oschinski, J. Beyer, S. Horn, L. Hörner, K. Santo, *Compatibility of Metals, Alloys and Coatings with Static Pb–17Li Eutectic Mixture FZKA 5596*, Forschungszentrum Karlsruhe, 1995.
- [34] M. Abdou, A. Ying, N. Morley, K. Gulec, S. Smolentsev, et al., *Fusion on Engineering and Design* 54 (2001) 181–247.
- [35] W.P. Jones, B.E. Launder, *International Journal of Heat Mass Transfer* 15 (1972) 301–314.
- [36] S. Smolentsev, M. Abdou, N. Morley, A. Ying, T. Kunugi, *International Journal of Engineering Science* 40 (2002) 693–711.
- [37] F.G. Blottner, *Computation Methodology of Applied Mechanical Engineering* 4 (1974) 179–194.
- [38] S. Smolentsev, M. Abdou, N.B. Morley, M. Sawan, S. Malang, C. Wong, *Fusion Engineering and Design* 81 (2006) 549–553.
- [39] M.J. Pattison, S. Smolentsev, R. Munipalli, M. Abdou, *Fusion of Science and Technology* 60 (2011) 809–813.
- [40] D.W. Peacaman, H.H. Rachford, *Journal of the Society for Industrial and Applied Mathematics* 3 (1955) 28–41.
- [41] R. Moreau, *Magneto hydrodynamics*, Kluwer Academic Publishers, Dordrecht, 1990.
- [42] R. Moreau, Y. Bréchet, L. Maniguet, *Fusion Engineering and Design* 86 (2011) 106–120.
- [43] S. Malang, R. Mattas, *Fusion Engineering and Design* 27 (1995) 399–406.
- [44] G. Rampal, A. Li Puma, Y. Poitevin, E. Rigal, J. Szczepanski, C. Boudot, *Fusion Engineering and Design* 75–79 (2005) 917–922.